Decoupled overlapping grids for the numerical modeling of oil wells

Ogbonna, Nneoma; Duncan, Dugald Black

Published in:
Journal of Computational Physics

DOI:
10.1016/j.jcp.2011.09.002

Publication date:
2012

Journal of Computational Physics 231 (2012) 135–151

Contents lists available at SciVerse ScienceDirect

Journal of Computational Physics

journal homepage: www.elsevier.com/locate/jcp

Decoupled overlapping grids for the numerical modeling of oil wells

Nneoma Ogbonna *, Dugald B. Duncan

Department of Mathematics, Heriot-Watt University, Edinburgh EH14 4AS, UK

ARTICLE INFO

Article history:
Received 27 November 2010
Received in revised form 31 August 2011
Accepted 2 September 2011
Available online 12 September 2011

Keywords:
Overlapping grids
Reservoir simulation
Numerical well test analysis

ABSTRACT

Accurate computation of time-dependent well bore pressure is important in well test analysis – a branch of petroleum engineering where reservoir properties are estimated by comparing measured pressure responses at an oil well to results from a mathematical model. Similar methods are also used in groundwater engineering. In this paper we present the new approach of decoupled overlapping grids for accurately computing time-dependent pressure at the oil well. Our method is implemented in two stages: a global stage with a simple point or line source well approximation, and a local post-process stage with the well modeled correctly as an internal boundary. We investigate the accuracy of our method for a representative 2D problem in both homogeneous and heterogeneous isotropic domains, and compare our results with the widely used Peaceman well index solution (in the homogeneous case), and the approximate solution on locally refined grids. We also present a theoretical analysis that explains the observed $\mathcal{O}(h^2)$ behavior of the error in our method for the homogeneous case.

1. Introduction

Mathematical models that can accurately reproduce dynamic early-time pressure behavior at the well bore are important in well test analysis. Well test analysis is a reservoir assessment technique used to estimate reservoir properties, for instance reservoir size and permeability, and well bore properties like effective well radius and exact well location. The process involves matching field measurements of the pressure response due to changing production or injection rates taken at well bore to the output of a mathematical model. An introduction to well test analysis can be found in standard texts like [1–3].

Transient well test analysis uses a broad spectrum of models, ranging from the linear pressure equation in homogeneous reservoirs through to full multiphase flow in reservoirs with the heterogeneous "highly detailed medium parameters" of [4]. However, much (perhaps most) practical transient well test analysis is based on the linear pressure equation in a homogeneous or mildly heterogeneous medium. Established well testing techniques rely heavily on analytic models. For example, the exponential integral function solution for the pressure generated by a fully penetrating line source in a homogeneous infinite reservoir appears in many standard texts on well test analysis. This model is usually combined with the method of images to account for the reservoir boundaries. Another method often used to model arbitrary well configurations is the integration of appropriate source functions along the well length, as seen in [5–10]. However these models are derived for simple reservoir properties and shapes, and are difficult to adapt to the complex heterogeneity and geometry of realistic reservoirs.

An alternative approach is to match the measured pressure response to the well bore pressure from a numerical simulation. This offers more flexibility as complex reservoir features can be incorporated into the numerical simulation. One difficulty in this approach comes from the difference in scale between the diameter of a well bore (~10 cm) and the size

* Corresponding author. Tel.: +44 1235 559595.
E-mail address: nneoma08@yahoo.com (N. Ogbonna).

0021-9991/$ - see front matter © 2011 Elsevier Inc. All rights reserved.
doi:10.1016/j.jcp.2011.09.002

of a reservoir (typically $\mathcal{O}(1) - \mathcal{O}(10)$ km). Pressure gradients are largest in the region closest to the well bore, and this region is typically smaller than the spatial size of the grid blocks used in reservoir simulation. Standard reservoir simulations approximate a well by a point source (in 2D) or a line source (in 3D) and then post-process the results to get the pressure at the well bore surface. The Peaceman [11,12] well index is the widely accepted standard for computing steady-state well bore pressure from coarse grid simulations, but it performs poorly for initial transient well bore pressure. Transient well index models such as in [13,14], and by Peaceman [11], extend the steady-state Peaceman well index concept to computing early-time dynamic well bore pressure. Because these models rely on analytic solutions, they can be difficult to formulate for general heterogeneous bounded reservoirs.

It is also possible to model the full detail of the reservoir and well bore in a finite element approximation, using a highly refined mesh in the well vicinity. However this would significantly increase computational cost since many model evaluations are usually required in the parameter fitting process involved in well test analysis, and the computational mesh would have to be regenerated in the entire domain to deal with model parameter changes in well properties such as radius, location or orientation. This is especially true for 3D field-scale simulations with a large number of wells.

The method of decoupled overlapping grids presented in this work is an attractive alternative to the well modeling techniques described above. A schematic representation of the method for a 2D problem is shown in Fig. 1. The method is implemented in two stages. In the first (global) stage, the problem is solved in the entire reservoir with the well approximated by a point source or a line source. This stage can be implemented in standard reservoir simulators. In the second (local) stage, the problem is solved in a smaller near-well region with the well modeled as an internal boundary. This stage is a post-process stage since it carried out at the end of the first stage, and the local domain external boundary data is interpolated from the first stage results. This is conceptually similar to Peaceman post-processing, but it is much more flexible since there are no built-in assumptions about the form of the solution or properties of the medium in the vicinity of the well. Note that the shapes of the domains and their grids in Fig. 1 are for illustration and various types are used in practice.

The method of decoupled overlapping grids offers advantages over analytic well models and numerical well modeling by local grid refinement. First, since a fine local mesh can be fitted to the well bore, we are able to recover the high level of accuracy associated with analytic and locally refined numerical models. However while the analytic models are restricted to simple reservoir configurations, the method of decoupled overlapping grids, being purely a numerical model, can be applied to any well configuration and reservoir geometry and heterogeneity. Second, by decoupling the local fine mesh calculations from the global simulation, we are able to modify the properties of the well, like well location and shape, without the need to regenerate the mesh in the entire reservoir domain, in contrast to well modeling by local grid refinement. Third, both global and local effects are accurately accounted for. Complex reservoir features can be incorporated into the computations in a fast and efficient manner by solving the first stage in already existing reservoir simulators built for this purpose, while locally varying well properties which are of a significantly smaller spatial scale than can be captured by these reservoir simulators are incorporated into the post-process stage. The decoupling of global and local simulations also has the advantage that the local stage can be implemented as an add-on to existing reservoir simulators to improve results in the near-well region, and the local stage mesh can be easily adapted to the well shape for accurate and efficient computation of solutions.

Our method is different from the traditional composite overlapping grids method in the literature, for example in [15–17]. In composite overlapping grids, the equations are solved simultaneously on a grid system composed of component meshes that overlap in some regions. Duncan and Qiu [17] applied the composite overlapping grids method to solve the pressure equation within the context of well test analysis. They gave theoretical proofs of stability and convergence for a 1D problem, and demonstrated numerically that convergence for a 2D problem appears to behave in a similar manner as the 1D problem.

A key feature of the method in this paper is that data at the external boundary of the post-process stage is obtained from a global simulation where the well is modeled as a point or line source. The error in this boundary data as a result of the well approximation is the modeling error, and it decreases with increased distance away from the point source, as will be shown in Section 3. So by measuring at a sufficient distance away from the point source, the modeling error in the external boundary data of the post-process stage can be kept within acceptable bounds. A possible alternative approach to reducing the modeling error is to iterate the first and second stage processes, but we have not investigated this. Apart from the modeling

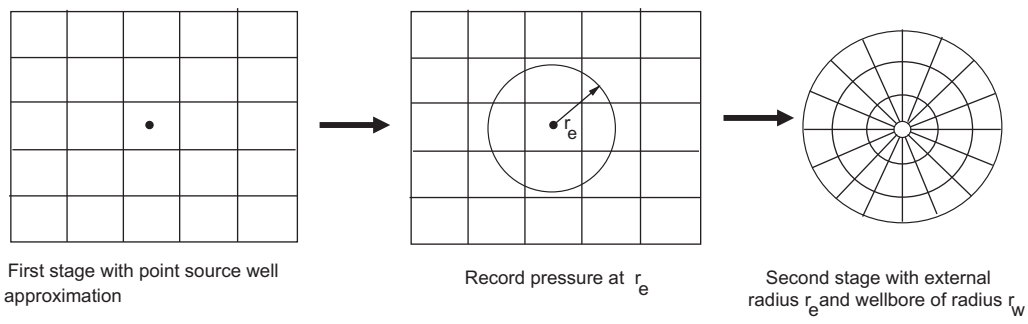

Fig. 1. Schematic representation of decoupled overlapping grids method for the model problem.

error, the numerical methods that are used in the first and second stage simulations also contribute to the final error in the well bore pressure. We will refer to the error contribution from the numerical methods as the numerical error.

We will restrict our discussion to a 2D domain. We start by describing the model problem and its analytic solution. We then investigate the error in the method by considering numerical examples in homogeneous and heterogeneous domains. We also present a theoretical analysis of the observed error convergence behavior for the transient problem in a homogeneous domain.

2. Governing equations

A schematic representation of the proposed method for a 2D problem is shown in Fig. 1. In the global (first stage) simulation the well is approximated by a point source. We assume a no-flow outer boundary condition for the global domain. During the global stage simulation, the time-dependent pressure is recorded at the points corresponding to the outer boundary of the local second stage simulation domain. These recorded data form the external boundary data for the local (second stage) simulations.

We assume single-phase slightly compressible fluid flow. For a homogeneous, isotropic reservoir, and a well producing at constant rate, the global (first stage) equations are:

$$\frac{1}{\eta}\frac{\partial p_{\mathrm{ps}}}{\partial t}(\mathbf{x},t) = \nabla^2 p_{\mathrm{ps}}(\mathbf{x},t) + Q\delta(\mathbf{x}-\mathbf{x}_0), \quad \text{in } \Omega\times(0,T], \tag{1a}$$

$$\frac{\partial p_{\mathrm{ps}}}{\partial n}(\mathbf{x},t) = 0, \quad \text{in } \partial\Omega\times(0,T], \tag{1b}$$

$$p_{\mathrm{ps}}(\mathbf{x},0) = 0, \quad \text{in } \Omega. \tag{1c}$$

Here Ω is the global computational domain, p_{ps} represents the pressure draw-down for a point source well, η is the diffusivity coefficient, δ is the Dirac delta function with $\mathbf{x}_0$ representing the point source location, and $Q = q\mu/k$ is the scaled flow rate at the well bore (k is the domain permeability and μ is the fluid viscosity). The normal direction in (1b) is out of Ω. Likewise the local (second stage) equations are:

$$\frac{1}{\eta}\frac{\partial p_{\mathrm{fw}}}{\partial t}(\mathbf{x},t) = \nabla^2 p_{\mathrm{fw}}(\mathbf{x},t), \quad \text{in } \Gamma\times(0,T], \tag{2a}$$

$$\frac{\partial p_{\mathrm{fw}}}{\partial n}(\mathbf{x},t) = -\frac{Q}{|\partial\Gamma_w|}\left(= -\frac{Q}{2\pi r_w}\right), \quad \text{in } \partial\Gamma_w\times(0,T], \tag{2b}$$

$$p_{\mathrm{fw}}(\mathbf{x},t) = p_{\mathrm{ps}}(\mathbf{x},t), \quad \text{in } \partial\Gamma_o\times(0,T], \tag{2c}$$

$$p_{\mathrm{fw}}(\mathbf{x},0) = 0, \quad \text{in } \Gamma. \tag{2d}$$

Here p_{fw} is the pressure draw-down for a well of finite diameter, and Γ is the local post-process domain with the internal (well) and external domain boundaries represented by $\partial\Gamma_w$ and $\partial\Gamma_o$ respectively. The normal direction in (2b) is out of the well. In this work wells are assumed to be of circular cross-section. Hence in (2b), $|\partial\Gamma_w| = 2\pi r_w$ where r_w is the radius of the well bore.

In the rest of the paper we set $\eta = 1$, $Q = 1$ without loss of generality, and carry out illustrative calculations on a unit square domain Ω with well radius $r_w = 10^{-3}$.

3. Analytic solution

We begin with a discussion of analytic solutions for two reasons. First, a comparison of the analytic solutions for the point source well and the finite radius well problems demonstrates the modeling error. Second, the analytic solutions discussed here are the benchmark for the numerical example in Section 4.

The analytic solution in Ω (unit square) will be obtained by applying the method of images to the infinite domain solutions which we give next. A point source well producing at a constant rate in an infinite, homogeneous, isotropic domain induces a radially symmetric pressure distribution described by:

$$\frac{1}{\eta}\frac{\partial p_{\mathrm{ps}}}{\partial t} = \frac{\partial^2 p_{\mathrm{ps}}}{\partial r^2} + \frac{1}{r}\frac{\partial p_{\mathrm{ps}}}{\partial r}, \tag{3a}$$

$$p_{\mathrm{ps}}(r,0) = 0, \tag{3b}$$

$$p_{\mathrm{ps}}(r\to\infty,t) = 0, \tag{3c}$$

$$2\pi\lim_{r\to 0}\left(r\frac{\partial p_{\mathrm{ps}}}{\partial r}\right) = -Q. \tag{3d}$$

The solution to (3) is the well known exponential integral function:

$$p_{\mathrm{ps}}(r,t) = -\frac{1}{2}\left[\frac{Q}{2\pi}\,\mathrm{Ei}\left(-\frac{r^2}{4\eta t}\right)\right]. \tag{4}$$

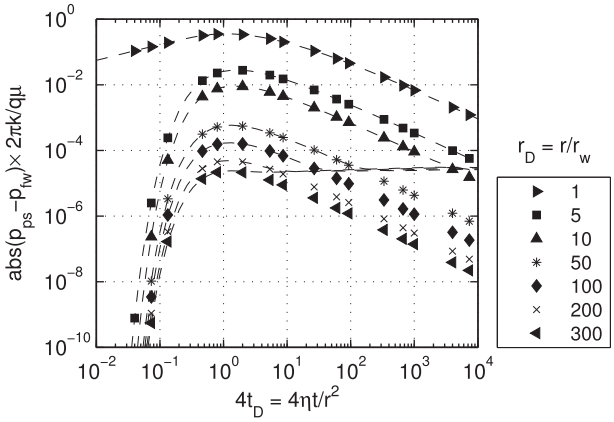

Fig. 2. Absolute error in pressure draw-down against dimensionless time. Markers: Infinite domain. Lines: Finite domain.

Likewise for a well of finite radius r_w, we have the following equations:

$$\frac{1}{\eta}\frac{\partial p_{\mathrm{fw}}}{\partial t} = \frac{\partial^2 p_{\mathrm{fw}}}{\partial r^2} + \frac{1}{r}\frac{\partial p_{\mathrm{fw}}}{\partial r}, \tag{5a}$$

$$p_{\mathrm{fw}}(r,0) = 0, \tag{5b}$$

$$p_{\mathrm{fw}}(r\to\infty,t) = 0, \tag{5c}$$

$$\frac{\partial p_{\mathrm{fw}}}{\partial r}(r_w,t) = -\frac{Q}{2\pi r_w}. \tag{5d}$$

A closed form solution is given in [2], but it is very difficult to evaluate or to approximate and we instead use Laplace transform methods. In Laplace space:

$$\hat{p}_{\mathrm{fw}}(r,s) = \frac{Q}{2\pi}\left(\frac{\sqrt{\eta}K_0\left(r\sqrt{s/\eta}\right)}{r_w(\sqrt{s})^3 K_1(r_w\sqrt{s/\eta})}\right), \tag{6}$$

where s is the Laplace transform variable and K_0, K_1 are modified Bessel functions of the second kind. The numerical inversion of (6) to the real time domain is carried out using the Iseger [18] algorithm , which is very accurate.

The modeling error in the pressure at fixed radii from the well is plotted in Fig. 2. The markers represent the modeling error in an infinite domain, while the broken lines represent the modeling error in the finite (unit square) computational domain Ω with the well at its center. Fig. 2 shows that the error measured in both finite and infinite domains are the same initially since the influence of the boundary is insignificant at early times, but as the simulation progresses the error in the finite domain settles to a near-constant value due to boundary effects. The maximum error occurs during an initial transient phase except when the measurement radius is close to the domain boundary, in which case the initial transient phase is absent and the maximum error occurs at steady-state (see $r_D = 300$ in Fig. 2). Also it is seen that the maximum modeling error decreases as the measurement radius increases.

4. Numerical Example 1

For this example the well is located at the center of a unit square isotropic and homogeneous reservoir. The quantity of interest in the calculations is the spatially averaged well bore pressure, which is simply an average in the angle variable in standard 2D polar coordinates. The local second stage domain is the annulus illustrated in Fig. 1. For this and all the other numerical examples the equations are first semi-discretized in space, and then time integration is performed using `ode15s`, a Matlab variable order initial value ODE solver. More details of the two stages of the simulation are given below.

4.1. First stage simulation

The first stage equations in (1) are semi-discretized on a finite element mesh using linear Lagrange elements. The mesh is uniform, that is, there is no local refinement near the point source well. In addition the location of the point source is not constrained to a vertex, rather the vertices of the enclosing triangle are defined to be point sources whose strengths are weighted depending on the location of the point source.

At the end of the first stage simulation the average pressure is measured at fixed radii $r_e = 0.1, 0.2, 0.3$. These radii form the outer boundaries for the second stage simulations. The average pressure is calculated by first linearly interpolating the first stage solution to points on r_e and then taking the average.

Fig. 3 shows the maximum absolute error in the pressure at r_e taken over dimensionless time $4t_D \in [10^{-2}, 10^4]$ where $t_D = \eta t / r_e^2$. The maximum error is plotted against the degrees of freedom (d.o.f) of the underlying finite element mesh. The average pressure measurement at r_e is compared against the analytic point source solution in Section 3 to get the numerical error, and against the analytic finite radius well solution in Section 3 to get the sum of the modeling and numerical error. It is seen that the modeling error at these r_e is noticeable only for significantly fine mesh sizes. Also plotted in Fig. 3 is a line of slope -1, which by comparison indicates an $\mathcal{O}(h^2)$ convergence of the maximum absolute error at r_e, where h denotes the mesh size. A proof of this convergence rate is given in Section 7.1.

4.2. Second stage simulation

The computational domain for this example is the annulus illustrated in Fig. 1 and it is isotropic and homogeneous. Working in standard $r-\theta$ polar coordinates centered at the well, the quantity of interest is the angular (θ) average of the pressure at the well bore. Because of the properties of this domain, one can replace the full 2D problem in (2) by the equivalent 1D problem below for the angular average pressure at distance r from the well center. Note that this is not an essential part of the method, but, when it can be used for this and similar problems, it gives a cost saving.

To refine the grid near the well bore, the coordinate transformation

$$r \to \ln r \stackrel{def}{=} R \tag{7}$$

is applied. The transformation is chosen to accurately capture the steady state behavior [19], but more sophisticated mesh adaptation could of course be used in its place. Using (7) we have the following equations for the second stage:

$$\frac{1}{\eta}\frac{\partial p_{\mathrm{fw}}}{\partial t} = e^{-2R}\frac{\partial^2 p_{\mathrm{fw}}}{\partial R^2}, \quad R_w < R < R_e, \ t > 0, \tag{8a}$$

$$\frac{\partial p_{\mathrm{fw}}}{\partial R} = -\frac{Q}{2\pi}, \quad R = R_w, \ t > 0, \tag{8b}$$

$$p_{\mathrm{fw}}(R_e, t) = p_{\mathrm{ps}}(R_e, t), \quad R = R_e, \ t > 0, \tag{8c}$$

$$p_{\mathrm{fw}}(R, 0) = 0, \quad R_w < R < R_e, \tag{8d}$$

where $p_{\mathrm{ps}}(R_e, t)$ is the average pressure at radius R_e measured from the global solution. Space discretization of (8) is performed using the vertex-centered finite volume method.

Numerical experiments for different refinement levels of the radial mesh were carried out. From these we found that setting $\Delta r_{\max} = h$, where $\Delta r_{\max}$ is the maximum radial mesh size and h is the average triangle size of the underlying global simulation, gives maximum absolute errors in well bore and external boundary pressure that are within the same order of magnitude. The maximum absolute error in the well bore pressure is plotted in Fig. 4 against the number of radial grid points for $\Delta r_{\max} = h$, $h/2$, $h/4$. It is seen that while there is a marked decrease in the absolute error in refining from $\Delta r_{\max} = h$ to $\Delta r_{\max} = h/2$, there is little gain in accuracy in refining further to $\Delta r_{\max} = h/4$. Also shown in Fig. 4 is a line of slope -2 which by comparison indicates an $\mathcal{O}((\Delta r_{\max})^2)$ convergence of the maximum absolute error at r_w. A proof of this convergence rate is given in Section 7.2.

In Fig. 5 the absolute maximum error in the well bore pressure and external boundary pressure of the local domain are plotted against the degrees of freedom (d.o.f) of the underlying global FEM mesh. It can be seen that for $\Delta r_{\max} \leqslant h/2$, the error

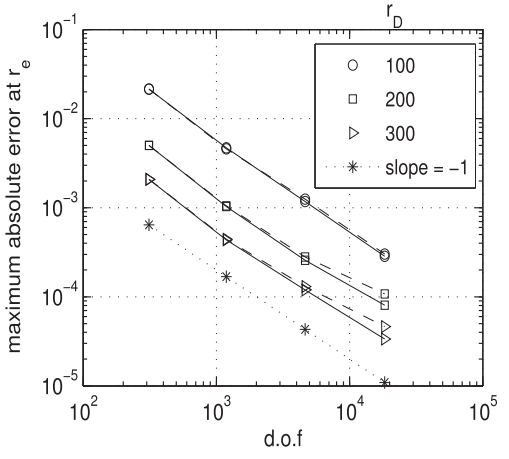

Fig. 3. Maximum absolute error in pressure drawdown at $r_D = r_e/r_w$. Analytic solution = point source well solution (solid lines) and finite radius well solution (broken lines).

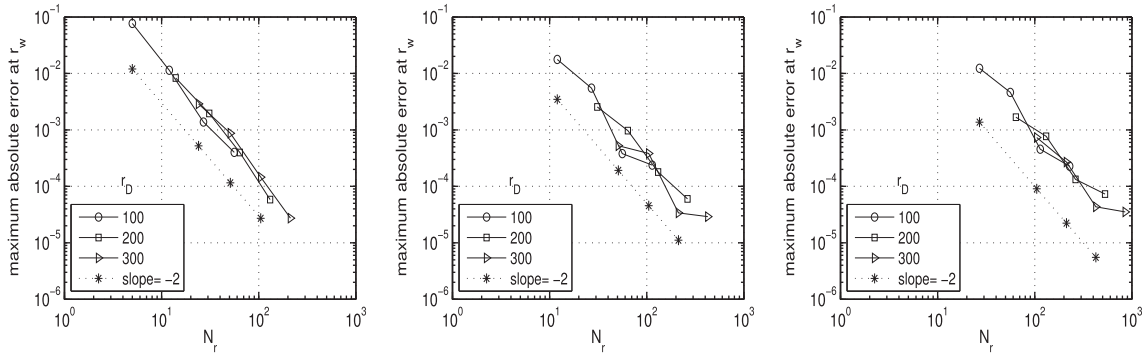

Fig. 4. Maximum absolute error in average well bore pressure over time interval $4t_D \in [10^{-2}, 10^4]$.

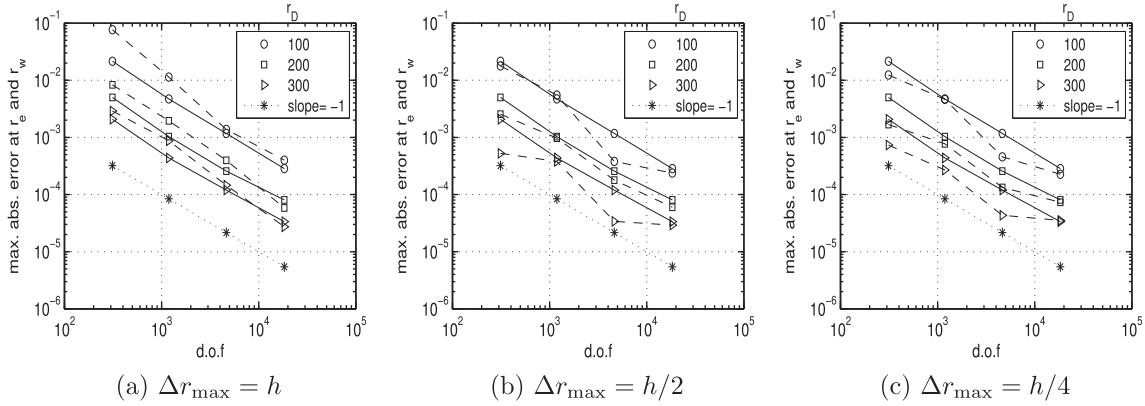

Fig. 5. Broken lines: Maximum absolute error in well bore pressure. Solid lines: Maximum absolute error in external boundary pressure. The maximum error is measured over time interval $4t_D \in [10^{-2}, 10^4]$.

in the well bore pressure is bounded above by the error in the external boundary pressure, Therefore as a guideline we propose that $\Delta r_{\max}$ should be set to $h/2$. We note here that the same trend was observed when the first stage was semi-discretized using the finite difference method on a rectangular mesh. This is the implementation often found in commercial reservoir simulators.

4.3. Comparison with solution on locally refined grids

We compare the well bore pressure calculated by decoupled overlapping grids to that calculated on two types of locally refined meshes. The first, shown in Fig. 6(a), is a triangular mesh with local grid refinement (LGR) used to resolve the well bore. Spatial discretization is by the finite element method using linear Lagrange elements. The second, shown in Fig. 6b, is a hybrid grid with a polar mesh close to the well bore and a rectangular mesh in the rest of the domain. Spatial discretization is by cell-centered finite volume method. The polar and rectangular sections of the mesh are connected by irregularly shaped blocks. This method was proposed by Pedrosa and Aziz [20] for use in reservoir simulation, and has been subsequently adopted in numerical reservoir simulation studies for instance in [21–23]. The benchmark solution is the analytic solution for a finite radius well calculated in Section 3.

A comparison of the maximum absolute error in well bore pressure for the locally refined meshes and the decoupled overlapping grids method is shown in Fig. 6c and d. For the decoupled overlapping grids solution in Fig. 6c, the first stage computation is on a triangular mesh using the finite element method (linear Lagrange elements) and in Fig. 6d, the first stage computation is on a rectangular mesh using cell-centered finite volume method. In both examples the second stage simulation is by the vertex-centered finite volume method. The external radius for the second stage simulation is $r_e = 0.1$ and the maximum mesh size $\Delta r_{\max} = h/2$. Note that $r_e = 0.1$ gives the least accurate results for the example in Section 4.2. For consistency, the radius of the largest circle in the polar inset of the hybrid grid is also set to 0.1. The plots in Fig. 6c and d clearly illustrate that the decoupled overlapping grids method performs significantly better for similar degrees of freedom.

The accuracy of the finite element solution with local refinement near the well bore can be improved by using quadratic Lagrange elements instead of linear Lagrange elements. Fig. 7 shows the absolute error in well bore pressure on a locally

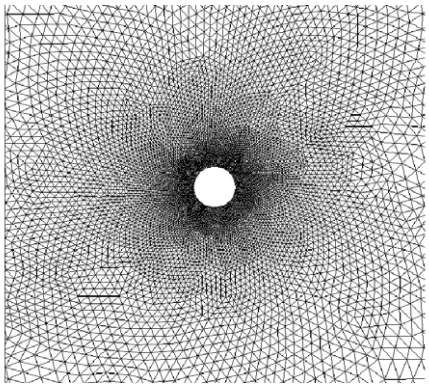

(a) Finite element mesh with local refinement near well bore.

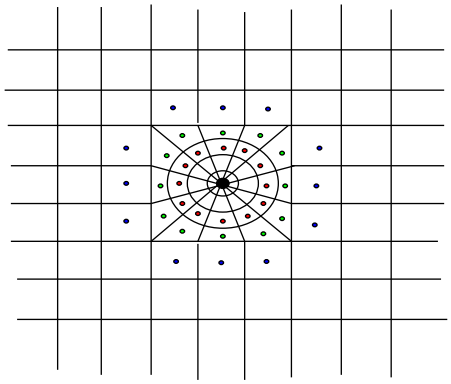

(b) Schematic representation of a hybrid grid.

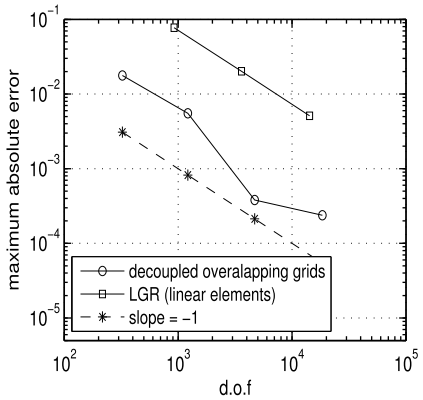

(c) Comparison with finite element method solution on mesh with LGR at well bore.

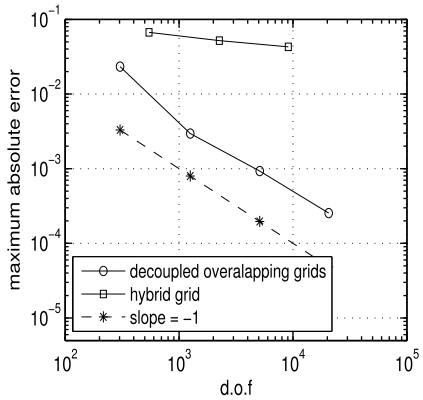

(d) Comparison with solution on hybrid grid.

Fig. 6. Maximum absolute error in average well bore pressure over time interval $4t_D \in [10^{-2}, 10^4]$. For decoupled overlapping grids simulation, $r_e = 0.1$ and $\Delta r_{\max} = h/2$.

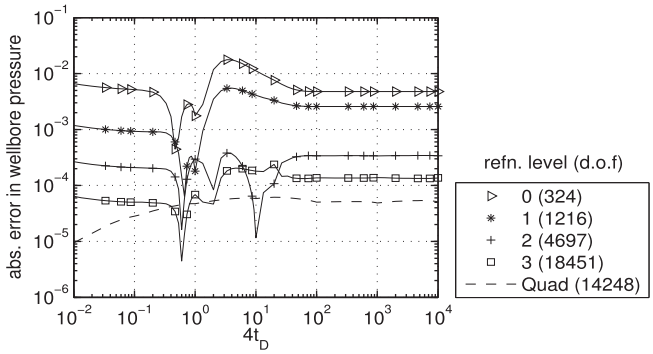

Fig. 7. Comparison with finite element method solution using quadratic Lagrange elements on mesh with LGR at well bore. For decoupled overlapping grids simulation, $r_e = 0.1$ and $\Delta r_{\max} = h/2$.

refined mesh using quadratic Lagrange elements, together with the absolute error in well bore pressure calculated by the decoupled overlapping grids method for different refinement levels of the underlying global mesh and with $r_e = 0.1$, $\Delta r_{\max} = h/2$. The quadratic Lagrange elements simulation has the same degrees of freedom as the most accurate point of the linear Lagrange FEM simulation in Fig. 6c.

Although the solution from quadratic Lagrange elements is very accurate as seen in Fig. 7, this method could potentially become highly computationally intensive for a well test study. For instance a change in well position will require a regeneration of the mesh in the entire simulation domain for a well bore resolved by local grid refinement. On the other hand for the decoupled overlapping grids method only the position of the point source need be changed in the global problem, together with a possible regeneration of the mesh on the significantly smaller local region surrounding the well bore for the post-process stage.

4.4. Comparison with Peaceman well index solution

The well index is used to calculate well bore pressure from well block pressure according to

$$p_w = p_b - \frac{q}{\mathrm{WI}}, \tag{9}$$

where p_w is the well bore pressure, p_b is the well block pressure and WI is the well index. The conventional well index proposed by Peaceman [11] for a fully-penetrating vertical well in a reservoir of thickness H takes the form

$$\mathrm{WI} = \frac{2\pi kH}{\ln \frac{r_{\mathrm{eq}}}{r_w}}, \tag{10}$$

where r_{eq} is an equivalent radius defined such that the pressure at this radius is equal to the numerically computed wellblock pressure. For a finite difference simulation on square gridblocks, Peaceman [11] gave the equivalent radius as:

$$r_{\mathrm{eq}} = 0.14\sqrt{2}\Delta x, \tag{11}$$

for steady-state flow and:

$$r_{\mathrm{eq}} = \Delta x \sqrt{\frac{4\eta t}{\Delta x^2} \exp\left(-\gamma - \frac{4\pi kH}{q\mu} p_b\right)} \tag{12}$$

for unsteady-state flow. In (12), $\gamma \approx 0.5772$ is Euler's constant and p_b is the well block pressure draw-down.

Fig. 8 shows a comparison of the maximum absolute error in well bore pressure calculated by the decoupled overlapping grids method and from the Peaceman well index with equivalent radius given in (11) and (12). The same global solution is used in all cases. This global solution is evaluated on a rectangular mesh using finite difference discretization in space. The benchmark solution is the analytic solution for a finite radius well calculated in Section 3.

For lines 2 and 3, the well bore pressure is calculated using the decoupled overlapping grids method with $\Delta r_{\max} = h/2$ and the external radius of the local post-process domain initially $r_e = 0.1$. For line 2, r_e remains constant as the underlying global grid is refined, while for line 3, $r_e = Ch$ as the underlying global grid is refined, where C is a positive constant.

For line 4 the well bore pressure is calculated from the Peaceman well index with r_{eq} given in (11). For line 5, the equivalent radius is given by (12) at early time and settles to (11) at steady-state. Also plotted in Fig. 8 is the maximum absolute error at r_e, and a line of slope = −1 which represents $\mathcal{O}(h^2)$ convergence rate.

Fig. 8 clearly shows the better performance of the decoupled overlapping grids method compared to the Peaceman well index solutions. For the decoupled overlapping grids simulation, an $\mathcal{O}(h^2)$ convergence of the maximum absolute error is observed for both well bore pressure and the pressure at the external boundary of the local domain when the size of the post-process domain $r_e = \mathcal{O}(1)$ as the global grid is refined. Also the maximum absolute error in the well bore pressure is bounded above by that of the external boundary pressure. On the other hand setting $r_e = \mathcal{O}(h)$ means that the error in the external boundary pressure gets worse as the global grid is refined since measurements are made closer to the point

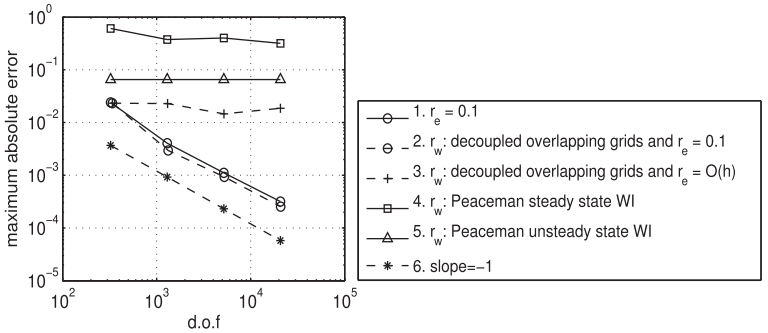

Fig. 8. Comparison of maximum absolute error in well bore pressure from the decoupled overlapping grids method and using Peaceman well index. Maximum taken over $4t_D \in [10^{-2}, 10^4]$.

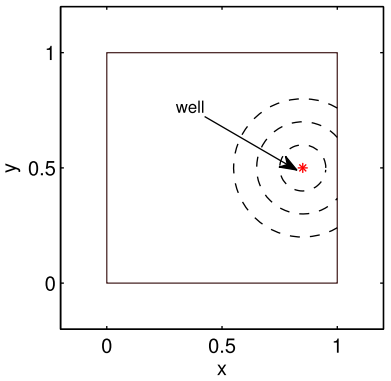

Fig. 9. Model problem. Well position: $(x_w, y_w) = (0.85, 0.5)$. Broken lines show post-process domain for $r_e = 0.1$, 0.2, 0.3.

source. From line 3 in Fig. 8, it is seen that the maximum absolute error in the well bore pressure remains fairly constant in this case, similar to the error obtained for the Peaceman well index calculations.

5. Numerical Example 2

In this example the well is moved close to the impermeable reservoir boundary, so that the post-process domain boundary intersects the global domain boundary. This example illustrates the relative ease with which the method of decoupled overlapping grids can be applied to compute transient well pressure in complex reservoir geometry. The principle extends to other similar problems such as a well close to a fault or a fracture.

We maintain the parameter values in the homogeneous case study in Section 4 with the exception of the well center which is now at $(0.85, 0.5)$. A representation of the model problem is shown in Fig. 9. As before the local post-process domain is defined from the center of the well bore to a fixed radius r_e. As shown in Fig. 9 the external boundary of the local domain is intersected by the global impermeable boundary when r_e is big enough and the local problem must be treated as fully 2D.

The local problem is solved in the transformed $\ln r - \theta$ coordinate system. The solution domain in this coordinate system is rectangular if the local domain is not intersected by the global domain boundary; otherwise it has a curved edge. Taking advantage of the symmetry of this case study along $y = 0.5$, the local solution is computed only in $\theta = 0{:}\pi$, applying a no-flow boundary condition at $\theta = 0$ and $\theta = \pi$. We semi-discretize both global and local problems using the finite element method on a triangular mesh, which is easy to adapt to the irregular shape of the local computational domain. Sample meshes in the transformed second-stage domain, together with the computed solution at the end of the simulations, are shown in Fig. 10.

A comparison of the maximum absolute error at the well bore and external boundary of the local domain is plotted in Fig. 11 against the degrees of freedom for the global stage simulation. Here h denotes the maximum mesh size in the global domain and $\Delta r_{\max}$ denotes the maximum mesh size in the original (untransformed) local domain. The error at the external

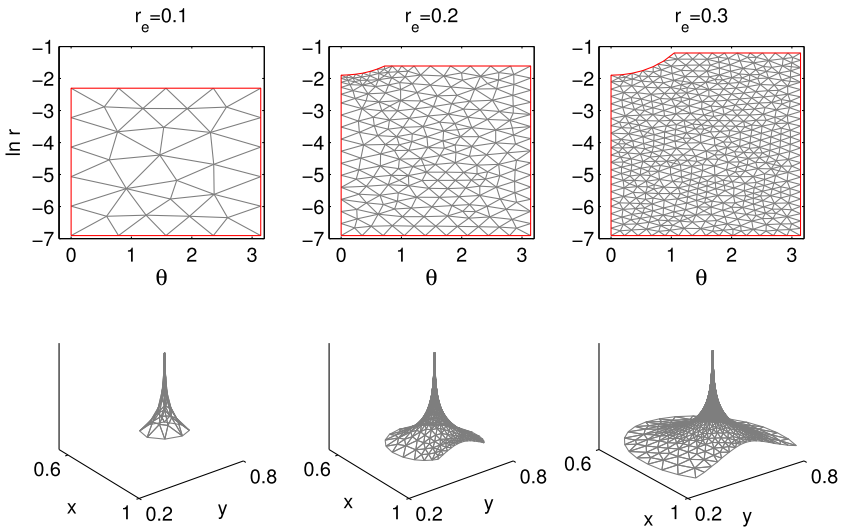

Fig. 10. Meshes in transformed local domain and approximate solution at end of the simulation. Global refinement level = 2, $\Delta r_{\max} = h$.

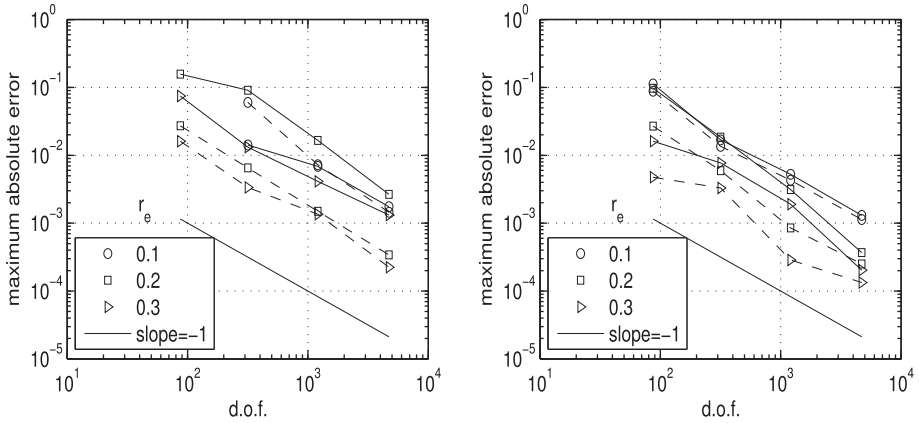

(a) $\Delta r_{\max} = h$ (b) $\Delta r_{\max} = \frac{h}{2}$

Fig. 11. Broken lines: Maximum absolute error in dimensionless well bore pressure. Solid lines: Maximum absolute error in dimensionless external boundary pressure. Maximum taken over simulation time $t_D \in [10^{-2}, 10^3]$.

boundary is computed only for the Dirichlet boundary portion, which has data interpolated linearly from the underlying global solution. The benchmark solution in this case is calculated on a locally refined finite element mesh using quadratic Lagrange elements. The plots show that for the irregular local domains ($r_e = 0.2, 0.3$), the maximum error in the well bore pressure is bounded above by the maximum error in the boundary pressure for $\Delta r_{\max} = h, h/2$. For $r_e = 0.1$ this property is true for $\Delta r_{\max} = h/2$, while for $\Delta r_{\max} = h$ the errors are within the same order of magnitude. The plots also show an $\mathcal{O}(h^2)$ convergence of the error. Therefore the results for a well near an impermeable boundary agree with those obtained for an isolated well in Section 4. Also out of the 23 simulations that were carried out for this case study, 17 had less than half the degrees of freedom of the benchmark solution, and the solution with the highest degree of freedom out of these 17 simulations comes within $\mathcal{O}(10^{-3})$ of the benchmark solution. Therefore a high level of accuracy can be achieved for significantly less computational effort.

6. Numerical Example 3

In this section, we apply the method of decoupled overlapping grids to domains with discontinuous permeability. We consider the following cases (shown in Fig. 12): radial, angular, and random permeability discontinuity. For the radially discontinuous case, a circular region extending a fixed radial distance from the center of the well is assigned a constant permeability k, and the region outside this circle is assigned a constant permeability k_2 where $k/k_2 = 0.1$. For the angular discontinuous case, the domain is divided into four quadrants. The north-east and south-west quadrants are assigned a constant permeability value k, and the north-west and south-east quadrants are assigned a constant permeability value k_2 where $k/k_2 = 0.1$. For the fully heterogeneous case, the domain is assigned an isotropic, correlated, log-normal random permeability distribution, which is a closer representation of a realistic reservoir permeability distribution. The permeability distribution is generated using the method outlined by Eberhard [24].

The well is located at the center of the unit square computational domain. In all cases the first stage simulation results are calculated as explained in Section 4.1, (again there is no local refinement near the point source well), and at the end of the first stage simulation the average pressure is measured at fixed radii $r_e = 0.1, 0.2, 0.3$. A full 2D simulation is used in the local, second stage calculations except in the special radial case. Simulation results are compared against benchmark solutions calculated on a finite element mesh (using quadratic Lagrange elements) that is locally refined around the well bore. Fig. 13 shows a comparison of maximum absolute error in the dimensionless average well bore pressure and dimensionless average external boundary pressure of the post-process domain, plotted against the degrees of freedom of the finite element mesh used to compute the global solution.

6.1. Radial discontinuity

For the radial permeability discontinuity case, the radius of the permeability discontinuity $r_k = 0.15$. The local problem satisfies the condition in Section 4 which allows it to be solved in one (radial) dimension only. The local equations are discretized using the finite volume method. In order to get consistent results, it is necessary for the location of the permeability discontinuity to coincide with a control volume interface.

The simulation results are shown in Fig. 13a. (No simulation was carried out when $\Delta r_{\max} > r_e$ or $\Delta\ r_{\max} > r_e - r_k$, hence some lines do not have data for coarser levels of refinement.) It is seen that for $\Delta r_{\max} \leqslant h/2$ the error in the well bore pressure

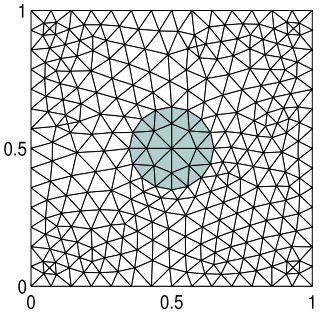

(a) Perm. inside circle $= k$, perm. outside circle $= k_2$, $k/k_2 = 0.1$.

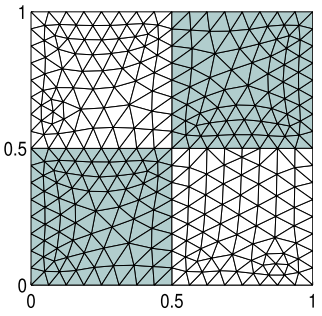

(b) Perm. in NE and SW quadrants $= k$, perm. in NW and SE quadrants $= k_2$, k/k_2=0.1.

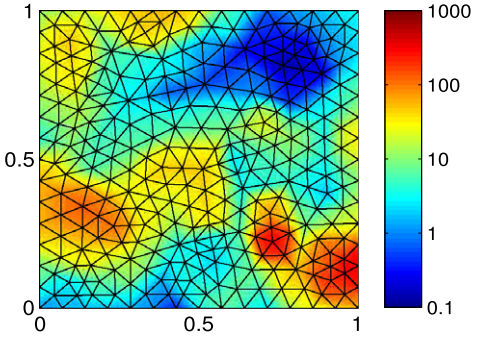

(c) Permeability values interpolated from triangle nodes

Fig. 12. Mesh for refinement level 2.

is bounded above by the error in the boundary condition. Even for $\Delta r_{\max} \approx h$, the maximum error in the well bore and boundary pressure are of similar magnitude (for refinement levels of the global simulation $\geqslant 1$). These results are similar to those observed for the homogeneous case study in Section 4. We also note that there is only a slight deterioration in the $\mathcal{O}(h^2)$ convergence rate that was observed for the homogeneous case. The most expensive computation using the decoupled overlapping grids method required a total degree of freedom that is only a third of that of the benchmark solution, and despite this significant difference in computational effort the solution comes within a dimensionless absolute error of $\mathcal{O}(10^{-4})$ with respect to the benchmark solution.

6.2. Angular discontinuity

For the angular permeability discontinuity case, a full 2D problem in $\ln r - \theta$ is solved in the circular post-process domain using the finite volume method. The simulation results are shown in Fig. 13b. The plot for $\Delta r_{\max} = h$ shows that the maximum error in well bore pressure is above that of the boundary pressure for all refinement levels of the underlying global simulation. Refining the mesh for the local problem by setting $\Delta r_{\max} = h/2$ results in maximum errors of similar magnitude, especially for $r_e = 0.2$ and 0.3. Further refinement to $\Delta r_{\max} = h/4$ yields better results, with the maximum error in well bore pressure strictly bounded above by the maximum error in boundary pressure for $r_e = 0.2$. An $\mathcal{O}(h^2)$ convergence rate is observed for the results.

Out of the 31 simulations that that were carried out for this case study, 26 had less than half the degrees of freedom of the benchmark solution. The solution with the highest degrees of freedom out of these 26 simulations comes within $\mathcal{O}(10^{-4})$ of the benchmark solution.

It is also interesting to note that the maximum absolute error in well bore pressure is bounded above by, or of a similar magnitude to, the maximum absolute error in boundary pressure for the local problem only when the plots of the absolute error versus time show the maximum occurring during an initial transient phase (in a similar manner to Figs. 2 and 7) for both global and local simulations. While most of the plots for the absolute error in boundary pressure over time show the characteristic property of reaching a maximum during an initial transient phase before settling to a steady-state value (with the exceptions occurring in the coarser simulation cases), the plots of the absolute error in the well bore pressure over time show this property only for the very refined grids. This is because the strong heterogeneity present at the well bore makes the use of a very fine mesh at the well bore necessary in order to obtain this property of the absolute error.

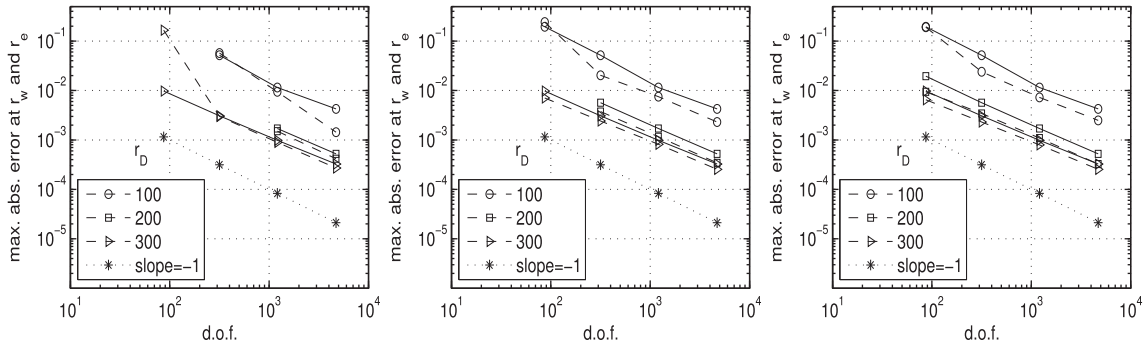

(a) Maximum absolute error for radial discontinuity (see Figure 12a).

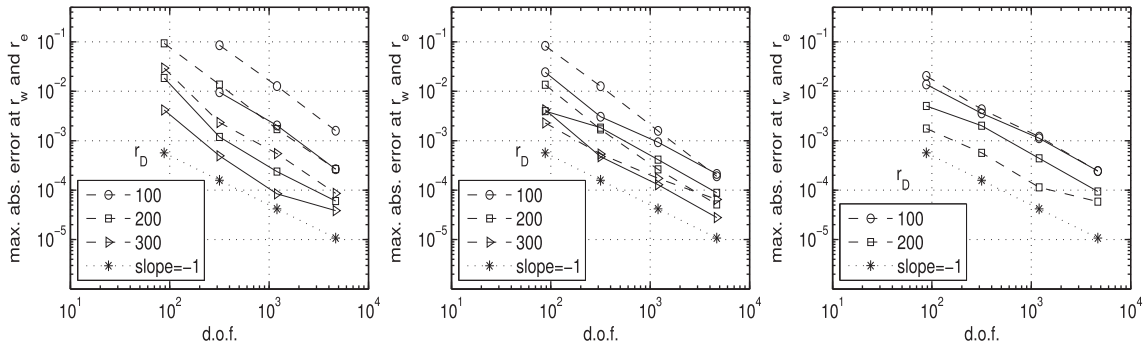

(b) Maximum absolute error for angular discontinuity (see Figure 12b).

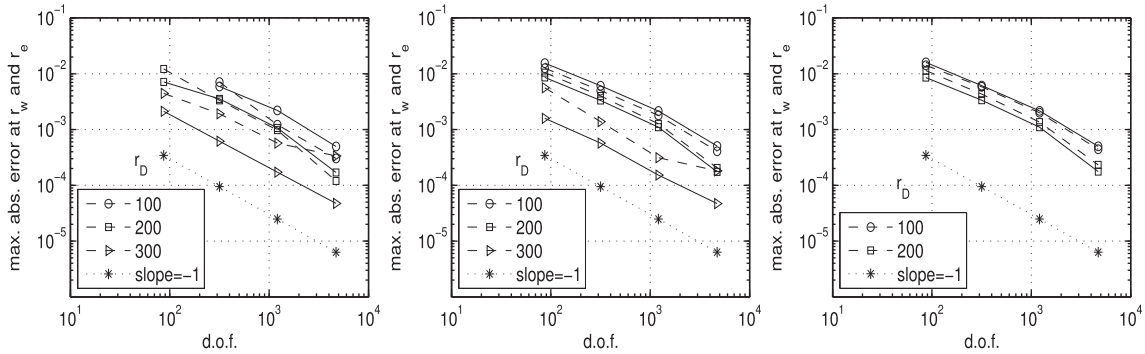

(c) Maximum absolute error for heterogeneous discontinuity (see Figure 12c).

Fig. 13. L → R: $\Delta r_{\max} = h, h/2, h/4$. Broken lines: Maximum absolute error in average well bore pressure. Solid lines: Maximum absolute error in average external boundary pressure. The maximum error is measured over time interval $4t_D \in [10^{-2}, 10^4]$.

6.3. Random permeability

For the random permeability discontinuity case, the original permeability distribution is generated at the vertices of the coarse mesh (refinement level 0), and extended to new vertices in subsequent refinement levels by linear interpolation. Also a full 2D problem in $\ln r - \theta$ is solved in the post-process stage using the finite volume method, with the permeability distribution interpolated linearly from the original coarse permeability distribution on refinement level 0. The simulation results shown in Fig. 12c show that with the exception of $r_D = 300$ (that is, $r_e = 0.3$), the maximum errors are within the same order of magnitude. A look at the absolute error plots over time revealed that although there is an initial transient period followed by a steady-state error, the maximum error hardly ever occurs during the initial transient phase. A possible reason for this is the fact all permeabilities are interpolated from a base coarse permeability distribution on refinement level 0, and so are approximations of the original rather than being exactly equal as in the previous case studies. Nevertheless, the maxima are not far apart, and Fig. 12c shows an $\mathcal{O}(h^2)$ convergence rate. (Also a comparison of the peak errors that occur

before steady-state is reached shows that the initial peak well bore error is bounded above by the initial peak error at the boundary.)

26 out of the 31 simulations that were carried out for this case study had less than half the degrees of freedom of the benchmark solution, still the solution with the highest degrees of freedom out of these 26 simulations comes within $\mathcal{O}(10^{-4})$ of the benchmark solution.

6.4. Discussion

The examples in this section show that the decoupled overlapping grids method can be used to accurately compute transient well bore pressure in the presence of some types of permeability heterogeneities within the reservoir. The simulation results support the suggestion in the previous sections of setting $\Delta r_{\max} = h/2$ to get a maximum error in average well bore pressure that is at least within the same order of magnitude as the maximum error in the average boundary pressure of the local post-process domain.

In these and more severe cases of heterogeneity, care must be taken to represent the geometry of the medium accurately enough in the local problem. Also, the interpolation from the global to local grid may have to cope with rapid changes in the global solution. This is partly addressed by having a fine enough local grid spacing on the outer boundary of the local problem, and some alignment of the local grid with the global is also advantageous. There is evidence from steady state problems in [19] that the $\ln r - \theta$ regular grid we have used gives good results unless the flow pattern around the well is very distorted by heterogeneity (say by high permeability channels). Then more sophisticated grid adaptation in the local problem will be required to achieve optimal results.

7. Theoretical analysis

The numerical results in Figs. 3 and 4 indicate an $\mathcal{O}(h^2)$ convergence of the maximum absolute error in the average pressure measured at a fixed radius from the point source in the first stage simulations and at the well bore in the second stage simulations respectively. In this section, theoretical error bounds for the maximum error in the first and second stage transient computations for homogeneous isotropic porous media are derived. They support the observed convergence behavior in the simulations. Dealing with the analysis when the porous media is highly heterogeneous would be much more difficult, and we note the sophisticated multiscale analysis in [4] for steady state problems in that case.

7.1. Finite element error in first stage

The global solution in Section 4.1 is obtained by solving the following equations:

$$\frac{\partial}{\partial t}p(\mathbf{x},t) - \nabla^2 p(\mathbf{x},t) = \delta(\mathbf{x}-\mathbf{x}_0), \quad \mathbf{x}\in\Omega,\ t>0, \tag{13a}$$

$$\nabla p(\mathbf{x},t)\cdot\mathbf{n} = 0, \quad \mathbf{x}\in\partial\Omega,\ t>0, \tag{13b}$$

$$p(\mathbf{x},0) = 0, \quad \mathbf{x}\in\Omega, \tag{13c}$$

where Ω is a bounded domain in $\mathbb{R}^2$. Let S_h^r denote a space of C^0 piecewise polynomial functions of degree $r-1 \geqslant 1$ on globally quasi-uniform partitions of Ω of mesh size h that fit the boundary exactly. The semi-discrete finite element approximation to (13) is:

$$\text{Find } p_h(t)\in C^0\left([0,T],S_h^r\right) \text{ such that}$$

$$(p_{h,t},\chi) + (\nabla p_h,\nabla\chi) = \chi(\mathbf{x}_0)\ \forall\chi\in S_h^r, t>0, \tag{14a}$$

$$\text{with } p_h(0) = 0\in S_h^r, \tag{14b}$$

where $(\cdot,\cdot)$ represents the $L_2(\Omega)$ inner product.

We wish to find error estimates $|(p-p_h)(\mathbf{x}^*,t^*)|$ at a fixed point away from the point of singularity $\mathbf{x}_0$. Maximum norm error estimates for parabolic initial boundary value problems with Neumann boundary conditions have been studied by Schatz et al. [25] and Leykekhman [26]. However their results do not directly apply here (see [27] for details). We instead write $p = U + G^{\mathbf{x}_0}$, where U is a smooth function and $G^{\mathbf{x}_0}$ is a Green's function that satisfy:

$$\frac{\partial}{\partial t}U(\mathbf{x},t) = \nabla^2 U(\mathbf{x},t), \quad \mathbf{x}\in\Omega, t>0, \tag{15a}$$

$$\nabla U(\mathbf{x},t)\cdot\mathbf{n} = 0, \quad \mathbf{x}\in\partial\Omega, t>0, \tag{15b}$$

$$U(\mathbf{x},0) = -G^{\mathbf{x}_0}(\mathbf{x}), \quad \mathbf{x},\mathbf{x}_0\in\Omega, \tag{15c}$$

and

$$-\nabla^2 G^{\mathbf{x}_0}(\mathbf{x}) = \delta(\mathbf{x}-\mathbf{x}_0), \quad \mathbf{x},\mathbf{x}_0\in\Omega, \tag{16a}$$

$$\nabla G^{\mathbf{x}_0}(\mathbf{x})\cdot\mathbf{n} = 0, \quad \mathbf{x}\in\partial\Omega,\mathbf{x}_0\in\Omega. \tag{16b}$$

The semi-discrete finite element approximation to p is then $p_h(t) = U_h(t) + G_h^{\mathbf{x}_0}$ where

$$(U_{h,t}, \chi) + (\nabla U_h, \nabla \chi) = 0, \quad \forall \chi \in S_h^r(\Omega), t > 0, \tag{17a}$$
$$U_h(0) = -G_h^{\mathbf{x}_0}, \tag{17b}$$

and

$$\left(\nabla G_h^{\mathbf{x}_0}, \nabla \chi\right) = \chi(x_0), \quad \forall \chi \in S_h^r(\Omega). \tag{18}$$

So

$$\begin{aligned} |(p - p_h)(\mathbf{x}^*, t^*)| &= |(U - U_h)(\mathbf{x}^*, t^*) + \left(G^{\mathbf{x}_0} - G_h^{\mathbf{x}_0}\right)(\mathbf{x}^*)| \\ &\leqslant |(U - U_h)(\mathbf{x}^*, t^*)| + |\left(G^{\mathbf{x}_0} - G_h^{\mathbf{x}_0}\right)(\mathbf{x}^*)|. \end{aligned} \tag{19}$$

We consider $|(U - U_h)(\mathbf{x}^*, t^*)|$ and $|\left(G^{\mathbf{x}_0} - G_h^{\mathbf{x}_0}\right)(\mathbf{x}^*)|$ independently by applying theorems by Solo [28] and Schatz and Wahlbin [29] respectively. We briefly state the theorems below for completeness.

7.1.1. Localised interior estimate for parabolic problems [28]

Let Ω be a bounded domain in $\mathbb{R}^N$, $Q = \Omega \times [0, T]$, and $\partial Q = \partial\Omega \times [0, T]$. Given the problem

$$\frac{\partial u}{\partial t} - \nabla^2 u = 0 \quad \text{in } Q, \tag{20a}$$
$$\mathbf{n} \cdot \nabla u = g \quad \text{on} \quad \partial Q, \tag{20b}$$
$$u(t = 0) = u_0 \quad \text{in } \Omega, \tag{20c}$$

where both g and u_0 in general have low regularity ($u_0 \in W_q^{-s}(\Omega), g \in W_q^{-k,-l}(\partial Q)$ for arbitrary s, k, l, and q), and its semi-discrete finite element approximation:

$$\begin{aligned} &\text{Find } u_h(t) \in C^0\left([0, T], S_h^r\right) \text{such that} \\ &(u_{h,t}, \chi)_\Omega + (\nabla u_h, \nabla \chi)_\Omega = \langle g, \chi \rangle_{\partial\Omega} \quad \forall \chi \in S_h^r \text{ and a.e in } [0, T], \end{aligned} \tag{21a}$$
$$u_h(0) = P_h u_0, \tag{21b}$$

where $P_h f$ is the L_2 projection onto S_h^r, and $\langle \cdot, \cdot \rangle$ denotes the pairing of a linear space with its dual, then the following theorem holds.

Theorem 1. *Assume S_h^r satisfies the required technical properties of the finite element space stated in [28] and that the triangulations fit the boundary exactly. Then for u and u_h defined above, if $x^* \in \Omega$, dist $(x^*, \partial\Omega) > d$ and $t^* > d^2$ for $d > ch$, the following estimate holds for any l and $k = 0, 1$:*

$$|(u - u_h)(x^*, t^*)| \leqslant C_{l,d} h^{r-k} \left(\|u_0\|_{W_1^{-k}(\Omega)} + \|g\|_{W_1^{-k-l}(\partial Q)} \right) \tag{22}$$

where $C_{l,d} = \log(1/d) d^{-N-r-2l}$.

7.1.2. Pointwise interior error estimates for the Green's function near the singularity [29]

Let Ω be a bounded domain in $\mathbb{R}^N$ with smooth boundary $\partial\Omega$, and A a bilinear form of type

$$A(u, v) = \int_\Omega \left(\sum_{i,j=1}^N a_{ij}(x) \frac{\partial u}{\partial x_i} \frac{\partial v}{\partial x_j} + \sum_{i=1}^N b_i(x) \frac{\partial u}{\partial x_i} v + d(x) u v \right) dx, \tag{23}$$

where A is coercive over H^1, that is, there exists a constant $c > 0$ such that

$$c \|u\|_{H^1(\Omega)}^2 \leqslant A(u, u) \quad \forall u \in H^1(\Omega). \tag{24}$$

Let $S_h(\Omega)$ be a one-parameter family of subspaces of $W_\infty^1(\Omega)$ that satisfy

$$\inf_{\chi \in S_h(\Omega)} \|u - \chi\|_{H^1(\Omega)} \leqslant C h^{l-1} \|u\|_{H^l(\Omega)} \quad \text{for } 1 \leqslant l \leqslant r. \tag{25}$$

Let $x_0 \in \Omega$, and $G^{x_0}(x), G_h^{x_0}(x)$ be the Green's function and approximate Green's function respectively which satisfy:

$$A(G^{x_0}, u) = u(x_0) \quad \forall u \in W_\infty^1(\Omega), \tag{26}$$
$$\text{and} \quad A\left(G_h^{x_0}, \chi\right) = \chi(x_0) \quad \forall \chi \in S_h(\Omega). \tag{27}$$

Then the following theorem holds.

Theorem 2. *Given the assumptions above, let $\Omega_1 \subset\subset \Omega_2 \subset\subset \Omega$. There exist constants C and C_2 so that if h is sufficiently small, then for $x_0 \in \Omega_1$ and $x \in \Omega_2$*

$$\text{If} |x - x_0| \geqslant C_2 h, \quad |\left(G^{x_0} - G_h^{x_0}\right)(x)| \leqslant \frac{C h^r}{|x - x_0|^{N+r-2}} \left(\ln \frac{|x - x_0|}{h} \right)^\alpha \tag{28}$$

$$\text{If } 0 \leqslant |x - x_0| \leqslant C_2 h, \quad |(G^{x_0} - G_h^{x_0})(x)| \leqslant C \begin{cases} \ln \frac{1}{|x-x_0|} + 1 & \text{for } N = 2 \\ \ln \frac{1}{|x-x_0|^{N-2}} & \text{for } N \geqslant 2 \end{cases} \tag{29}$$

where r is the optimal order of h, and α = 1 for r = 2, α = 0 for r ⩾ 3.

We note here that S_h^r, the space of continuous piecewise polynomial functions in (14), satisfies the technical properties of the finite element space required by Theorems 1 and 2.

Applying Theorem 1 for $l = 0$, $k = 0$, $r = 2$, $N = 2$, the following error estimate is obtained for U (see (15)):

$$|(U - U_h)(\mathbf{x}^*, t^*)| \leqslant \log(1/d) d^{-4} h^2 \|G^{\mathbf{x}_0}(\mathbf{x})\|_{L_1(\Omega)} \tag{30}$$

$$\leqslant C_1 \log(1/d) d^{-4} h^2 \tag{31}$$

since the L_1 norm of $G^{\mathbf{x}_0}(\mathbf{x})$ is bounded.

Applying Theorem 2 for $N = 2$, $r = 2$, the following error estimate is obtained for $G^{\mathbf{x}_0}$ (see (16)):

$$|(G^{\mathbf{x}_0} - G_h^{\mathbf{x}_0})(\mathbf{x}^*)| \leqslant C_2 h^2 \left(\ln \frac{|\mathbf{x} - \mathbf{x}_0|}{h} \right) |\mathbf{x} - \mathbf{x}_0|^{-2}. \tag{32}$$

So from (19), (31) and (32),

$$|(p - p_h)(\mathbf{x}^*, t^*)| \leqslant h^2 \left[C_1 \log(1/d) d^{-4} + C_2 \left(\ln \frac{|\mathbf{x} - \mathbf{x}_0|}{h} \right) |\mathbf{x} - \mathbf{x}_0|^{-2} \right] \tag{33a}$$

$$\leqslant h^2 (C_U + C_{G^{\mathbf{x}_0}}). \tag{33b}$$

(33) gives the pointwise error estimate for (13). It predicts $\mathcal{O}(h^2)$ behavior subject to C_U and $C_{G^{\mathbf{x}_0}}$. Since the pointwise error is $\mathcal{O}(h^2)$ at time t^*, the average error at a radius r_e away from the point source is also $\mathcal{O}(h^2)$ at t^*. Furthermore the maximum error of the average pressure at the radius r_e over the simulation time is also $\mathcal{O}(h^2)$. This supports the observed results in Section 4.1.

The form of the constant $C_{G^{\mathbf{x}_0}}$ implies that the pointwise error is worse when measurements are made close to the point source, while the form of the constant C_U suggests that the pointwise error is worse for measurements taken close to the domain boundary. Numerical experiments were carried out which showed that for (13), C_U gives a particularly pessimistic error bound that is not observed in the numerical results for measurements taken close to the domain boundary. The error bound is pessimistic because Theorem 1 covers a more general problem with low regularity Neumann boundary data, whereas the global problem in this section has smooth Neumann boundary data. On the other hand the experiments showed that the error is worse for measurements closer to the singularity as predicted by $C_{G^{\mathbf{x}_0}}$.

7.2. Finite volume error in second stage

The local solution in Section 4.2 is obtained by solving the transformed equations:

$$\frac{\partial p}{\partial t} = e^{-2R} \frac{\partial^2 p}{\partial R^2}, \quad R_w < R < R_e, t > 0, \tag{34a}$$

$$\frac{\partial p}{\partial R} = -\frac{1}{2\pi}, \quad R = R_w, t > 0, \tag{34b}$$

$$p(R_e, t) = p_e(t) (= p_{\text{ps}}(R_e, t)), \quad R = R_e, t > 0, \tag{34c}$$

$$p(R, 0) = 0, \quad R_w < R < R_e, \tag{34d}$$

where $R = \ln r$. Let p_h be the semi-discrete approximation to p on a grid Ω_h, and u the restriction of p to Ω_h. Then we have:

$$\frac{dp_h}{dt} = Ap_h + f, \tag{35}$$

$$\frac{du}{dt} = Au + f + \sigma_h(t), \tag{36}$$

where $\sigma_h(t)$ is the local truncation error. The error in the spatial discretization is $\varepsilon(t) = u(t) - p_h(t)$. We show below that the pointwise error at the well bore has $\mathcal{O}(h^2)$ convergence.

Expanding the semi-discrete approximation (35) for (34) using the vertex-centered finite volume method, we have, for uniform mesh size h,

$$e^{2R_1} p'_{h,1}(t) = \frac{2}{h^2}(-p_{h,1}(t) + p_{h,2}(t)) + \frac{2}{h}\left(-\frac{1}{2\pi}\right), \tag{37a}$$

$$e^{2R_k} p'_{h,k}(t) = \frac{1}{h^2}(p_{h,k-1}(t) - 2p_{h,k}(t) + p_{h,k+1}(t)), \quad 2 \leqslant k \leqslant m-2 \tag{37b}$$

$$e^{2R_{m-1}} p'_{h,m-1}(t) = \frac{1}{h^2}(p_{h,m-2}(t) - 2p_{h,m-1}(t)) + \frac{1}{h^2} p_e(t). \tag{37c}$$

The truncation error $\sigma_h(t)$ is $\mathcal{O}(h^2)$ at all points except at $k = 1$ where

$$\sigma_{h,1}(t) = \frac{1}{3} h u_{RRR}(R_w, t) + \mathcal{O}(h^2). \tag{38}$$

Despite this $\mathcal{O}(h^2)$ convergence of the spatial discretization error $\varepsilon(t)$ at all points can be shown using the theorems by Hundsdorfer and Verwer [30] on refined global error estimates and the logarithmic matrix norm. We briefly state these theorems below for completeness.

Theorem 3 (Refined global error estimates [30, p. 85]). *Consider the linear semi-discrete system*

$$w'(t) = Aw(t) + f(t) \tag{39}$$

where A is an $m \times m$ matrix and $f(t) \in \mathbb{R}^m$ represents a source term and boundary conditions in the PDE, and assume that the stability condition

$$\|e^{tA}\| \leqslant K e^{\alpha t} \quad \text{for } 0 \leqslant t \leqslant T \tag{40}$$

holds on all grids Ω_h, where the constants $K \geqslant 1$ and $\alpha \in \mathbb{R}$ are both independent of h. Suppose that for $0 \leqslant t \leqslant T$ we can decompose the truncation error $\sigma_h(t)$ as

$$\sigma_h(t) = A\xi(t) + \eta(t) \quad \text{with} \quad \|\xi(t)\|, \|\xi'(t)\|, \|\eta(t)\| \leqslant Ch^r \tag{41}$$

and suppose that $\|\varepsilon(0)\| \leqslant C_0 h^r$, where C, $C_0 > 0$ are constants, and $\varepsilon(t)$ is the spatial discretization error. Then we have convergence of order r with the error bounds

$$\|\varepsilon(t)\| \leqslant \begin{cases} KC_0 e^{\alpha t} h^r + \left(1 + Ke^{\alpha t} + \frac{2K}{\alpha}(e^{\alpha t} - 1)\right) Ch^r & \text{if } \alpha \neq 0, 0 \leqslant t \leqslant T \\ KC_0 h^r + (1 + K + 2Kt) Ch^r & \text{if } \alpha = 0, 0 \leqslant t \leqslant T \end{cases} \tag{42}$$

where $\|\cdot\|$ is the discrete L_p-norm.

Theorem 4 (Logarithmic matrix norm [30, p.32]). *Let $A \in \mathbb{C}^{m \times m}$ and $\alpha \in \mathbb{R}$. We have*

$$\mu(A) \leqslant \alpha \iff \|e^{tA}\| \leqslant e^{t\alpha} \quad \forall t \geqslant 0 \tag{43}$$

where $\mu(A)$ is the logarithmic matrix norm and $\|\cdot\|$ is the discrete L_p-norm.

The logarithmic matrix infinity norm of A is defined as [30]

$$\mu_\infty(A) = \max_i \left(\text{Re } a_{ii} + \sum_{j \neq i} |a_{ij}| \right). \tag{44}$$

So for (37) we have $\mu_\infty(A) = 0$ which implies, from Theorem 4, that $\|e^{tA}\| \leqslant 1$.

Next we need to write the truncation error in the form $\sigma_h = A\xi(t) + \eta(t)$ (see (41)). Ignoring $\eta(t)$ which represents the $\mathcal{O}(h^2)$ terms in the truncation error and putting $\sigma_h = A\xi(t)$ gives, from (37) and (38),

$$\xi_1 - \xi_2 = C_1 h^3 \tag{45a}$$
$$\xi_{k-1} - 2\xi_k + \xi_{k+1} = 0 \tag{45b}$$
$$\xi_{m-2} - 2\xi_{m-1} = 0 \tag{45c}$$

where $C_1 = u_{RRR}(R_w, t)/6$. Solving (45b) with the ansatz $\xi = ar^n$ gives $r = 1$ twice so that $\xi_n = a + bn$. Applying the boundary conditions (45a) and (45c) gives $\xi_k = C(m - k)h^3$; therefore $\xi_k \leqslant Cmh^3 = Ch^2$ (since $h = 1/m$). So $\|\xi(t)\|_\infty, \|\xi'(t)\|_\infty, \|\eta(t)\|_\infty \leqslant Ch^2$. Since $\varepsilon(0) = 0$, we set $C_0 = 2C$ so that Theorem 3 gives

$$\|\varepsilon(t)\|_\infty \leqslant 2(2 + t)Ch^2. \tag{46}$$

Therefore

$$|\varepsilon_k(t)| \leqslant \|\varepsilon(t)\|_\infty \leqslant 2(2 + t)Ch^2, \tag{47}$$

and the pointwise error has $\mathcal{O}(h^2)$ convergence at $R = R_w$ (that is, $k = 1$). Since the pointwise error is $\mathcal{O}(h^2)$ at R_w, the error in the average pressure at R_w is also $\mathcal{O}(h^2)$. Furthermore the maximum error in the average pressure at R_w over the simulation time is also $\mathcal{O}(h^2)$. This supports the observed results in Section 4.2.

8. Conclusion

The descriptions and examples in this paper demonstrate the main idea and accuracy of the decoupled overlapping grids method for the well test problem in an isotropic 2D domain. The proposed method performed better than the widely used

Peaceman well index solutions and solutions on locally refined grids for the same spatial discretization method. An $\mathcal{O}(h^2)$ convergence of the maximum absolute error in the average well bore and external local domain pressure was observed numerically in a range of homogeneous and heterogeneous test cases, and proved by analysis for homogeneous problems. In addition the numerical results suggest that the maximum absolute error in the average well bore pressure is bounded above by the absolute maximum error in the average external local domain boundary pressure when the maximum mesh size in the post-process stage is smaller than half the average mesh size in the global stage simulation.

The method described in this paper can be extended to well test problems in three-dimensional heterogeneous domains, and some promising test results are shown in [27]. As mentioned earlier, the global stage can be solved in already existing reservoir simulators, which can incorporate complex reservoir features, and the post-process simulation domain can be fitted to the well geometry to give accurate and efficient pressure transient solutions at the well bore. We discuss the implementation details and results for these challenging applications in a different paper.

Highly heterogeneous porous media presents further challenges, and we have noted some outstanding issues for implementation and analysis in Sections 6.4 and 7 respectively.

References

[1] R.N. Horne, Modern Well Test Analysis: A Computer-Aided Approach, Petroway Inc., Palo Alto, CA, second edition, 1995.
[2] T.D. Streltsova, Well Testing in Heterogeneous Formations, John Wiley and Sons, New York, 1998, 1998. An Exxon Monograph.
[3] M.A. Sabet, Well Test Analysis, Gulf Publishing Company, Houston, TX, 1991.
[4] Z. Chen, X. Yue, Numerical homogenization of well singularities in the flow transport through heterogeneous porous media, Multiscale Model. Simul. 1 (2003) 260–303.
[5] A.C. Gringarten, H.J. Ramey, The use of source and Green's functions in solving unsteady-state problems in reservoirs, SPE J. 13 (1973) 285–296.
[6] A.J. Rosa, R. Carvalho, A mathematical model for pressure evaluation in an infinite-conductivity horizontal well, SPE Formation Eval. 4 (1989) 559–566.
[7] E. Ozkan, R. Raghavan, S.D. Joshi, Horizontal-well pressure analysis, SPE Formation Eval. 4 (1989) 567–575.
[8] M.J. Economides, C.W. Brand, T.P. Frick, Well configurations in anisotropic reservoirs, SPE Formation Eval. 11 (1996) 257–262.
[9] V.R. Penmatcha, K. Aziz, Comprehensive reservoir/wellbore model for horizontal wells, SPE J. 4 (1999) 224–234.
[10] L. Ouyang, K. Aziz, A general single-phase wellbore/reservoir coupling model for multilateral wells, SPE Reserv. Eval. Eng. 4 (2001) 327–335.
[11] D.W. Peaceman, Interpretation of well-block pressures in numerical reservoir simulation, SPE J. 18 (1978) 183–194.
[12] D.W. Peaceman, Interpretation of well-block pressures in numerical reservoir simulation with nonsquare grid blocks and anisotropic permeability, SPE J. 23 (1983) 531–543.
[13] G. Blanc, D.Y. Ding, A. Ene, T. Estebenet, D. Rahon, Transient productivity index for numerical well test simulations, Reservoir Characterization – Recent Advances, AAPG Memoir 71 (1999) 163–174.
[14] R.A. Archer, T.T. Yildiz, Transient well index for numerical well test analysis, Presented at SPE Annual Technical Conference and Exhibition, New Orleans, Louisiana, 2001. 71572-MS.
[15] G. Chesshire, W.D. Henshaw, A scheme for conservative interpolation on overlapping grids, SIAM J. Sci. Comput. 15 (1994) 819–845.
[16] W.D. Henshaw, On multigrid for overlapping grids, SIAM J. Sci. Comput. 26 (2005) 1547–1572.
[17] D.B. Duncan, Y. Qiu, Overlapping grids for the diffusion equation, IMA J Numer. Anal. 27 (2007) 550–575.
[18] P.D. Iseger, Numerical transform inversion using Gaussian quadrature, Probab. Eng. Inf. Sci. 20 (2006) 1–44.
[19] C. Axness, J. Carrera, M. Bayer, Finite-element formulation for solving the hydrodynamic flow equation under radial flow conditions, Comput. Geosci. 30 (2004) 663–670.
[20] O.A. Pedrosa, K. Aziz, Use of a hybrid grid in reservoir simulation, SPE Reserv. Eval. Eng. 1 (1986) 611–621.
[21] R. Vicente, C. Sarica, T. Ertekin, A numerical model coupling reservoir and horizontal well-flow dynamics: Transient behaviour of single-phase liquid and gas flow, SPE J. 7 (2002) 70–77.
[22] F. Dickstein, A.Q. Lara, C. Neri, A.M. Peres, Modeling and simulation of horizontal wellbore-reservoir flow equations, Presented at Latin American and Caribbean Petroleum Engineering Conference, Rio de Janeiro, Brazil, 1997. 39064-MS.
[23] P. Gui, L.B. Cunha, J.C. Cunha, A numerical two-phase flow model coupling reservoir and multi-segment horizontal well, Presented at SPE Rocky Mountain Oil & Gas Technology Symposium, Denver, Colorado, USA, 2007. 107989-MS.
[24] J.P. Eberhard, Simulation of lognormal random fields with varying resolution scale and local average for Darcy flow, Comput. Vis. Sci. 9 (2006) 1–10.
[25] A.H. Schatz, V. Thomée, L.B. Wahlbin, Stability, analyticity, and almost best approximation in maximum norm for parabolic finite element equations, Commun. Pure Appl. Math. 51 (1998) 1349–1385.
[26] D. Leykekhman, Pointwise localized error estimates for parabolic finite element equations, Numer. Math. 96 (2004) 583–600.
[27] N. Ogbonna, Decoupled Overlapping Grids for Modelling Transient Behaviour of Oil Wells, Ph.D. thesis, Department of Mathematics, Heriot-Watt University, 2010.
[28] A. Solo, Sharp estimates for finite element approximations to parabolic problems with Neumann boundary data of low regularity, BIT Numer. Math. 48 (2008) 117–137.
[29] A.H. Schatz, L.B. Wahlbin, Interior maximum norm estimates for finite element methods, Math. Comput. 31 (1977) 414–442.
[30] W. Hundsdorfer, J.G. Verwer, Numerical solutions of time-dependent advection–diffusion-reaction equations, Springer Series in Computational Mathematics, vol. 33, Springer-Verlag, Berlin, 2003.